

Development and Comparison of the Techniques for Solving the Inverse Problem in Photoacoustics

Mioljub Vojislav Nesic (✉ mioljub@gmail.com)

Vinca Institute of Nuclear Sciences <https://orcid.org/0000-0002-1170-210X>

Marica Popovic

Univerzitet u Beogradu Institut za nuklearne nauke Vinca

Katarina Djordjevic

Univerzitet u Beogradu Filzički Fakultet

Vesna Miletic

Filozofski fakultet Univerziteta u Istocnom Sarajevu

Miroslava Jordovic-Pavlovic

College of Applied Sciences, Užice, Serbia

Dragan Markushev

Univerzitet u Beogradu Institut za Fiziku

Slobodanka Galovic

Univerzitet u Beogradu Institut za nuklearne nauke Vinca

Research Article

Keywords: photoacoustic, inverse problem, semiconductors, minimum volume cell, neural networks, thermal diffusivity, linear coefficient of thermal expansion

Posted Date: March 11th, 2021

DOI: <https://doi.org/10.21203/rs.3.rs-267516/v1>

License:  This work is licensed under a Creative Commons Attribution 4.0 International License.

[Read Full License](#)

Version of Record: A version of this preprint was published at Optical and Quantum Electronics on July 6th, 2021. See the published version at <https://doi.org/10.1007/s11082-021-02958-0>.

Development and comparison of the techniques for solving the inverse problem in photoacoustic characterization of semiconductors

M. Nestic¹, M. Popovic¹, K. Djordjevic², V. Miletic³, M. Jordovic-Pavlovic⁴, D. Markushev⁵ and S. Galovic¹

¹University of Belgrade, Vinca Institute of Nuclear Sciences, national institute of the republic of Serbia, Belgrade, Serbia

²University of Belgrade, Faculty of Physics, Belgrade, Serbia,

³University of East Sarajevo, Faculty of Philosophy, Pale, Bosnia and Herzegovina

⁴College of Applied Sciences, Uzice, Serbia

⁵University of Belgrade, Institute of Physics, national institute of the republic of Serbia, Belgrade, Serbia

e-mail: mio@jub.nesic@vin.bg.ac.rs

ORCID: 0000-0002-1170-210X

Abstract: In this work, theoretically/mathematically simulated (TMS) model is presented for the photoacoustic (PA) frequency response of a semiconductor in a minimum volume PA cell. By analyzing of the TMS model, the influences of thermal diffusivity and linear coefficient of thermal expansion on silicon sample PA frequency response were investigated and two methods were developed for their estimation. The first one is a self consistent inverse procedure (SCIP) for solving the exponential problems of mathematical physics, based on regression. The second one, a well trained three-layer perceptron with back propagation, based upon theory of artificial neural networks (ANN), is developed and presented. These two inverse problem solving concepts are applied to thermo-elastic characterization of silicon, compared and discussed in the domain of semiconductor characterization.

Keywords: photoacoustic; inverse problem; semiconductors; minimum volume cell; neural networks; thermal diffusivity; linear coefficient of thermal expansion

Acknowledgements: Authors wish to acknowledge the support of the Ministry of Education and Science of the Republic of Serbia

Abbreviations

The following abbreviations are used in this manuscript:

TMS	theoretically/mathematically simulated models
PA	photoacoustic/photoacoustics
SCIP	self-consistent inverse procedure
ANN	artificial neural network
EM	electromagnetic
LED	light emitting diode
ROI	region of interest
MSE	mean-square-error

1. Introduction

Photoacoustics is a non-destructive experimental technique, being extensively developed over the last forty years and finding its application in the characterization and imaging of various materials and devices (Bialkowski 1996; Tam 1986; Vargas and Miranda 1988) The oldest and the most widespread PA technique is frequency gas-microphone method (Galovic et al. 2014; Rosencwaig and Gerscho 1976; Rousset et al. 1983), which has proven to be very efficient in determination of optical, thermal and elastic properties of semiconductors, semiconductor structures, metals, composite materials, ceramics, polymers, etc. (Balderas-Lopez and Mandelis 2001; Mansanares et al. 1991; Markushev et al. 2018; Nesic et al. 2018; Todorović and Nikolic 2000).

In frequency photoacoustics, the sample is illuminated by a monochromatic EM beam of harmonically modulated intensity. Part of the excitation energy is absorbed in the sample, and part of this absorbed energy is converted into heat through various de-excitation and/or relaxation processes, thus generating a harmonic heat source with frequency equal to the modulation frequency of the excitation beam. This heat source introduces a periodical perturbation in thermodynamic state of the sample, causing periodical temperature variations at sample surfaces, periodical surface displacements and sample bending. Due to adiabatic state change, thermally and mechanically induced periodical pressure build-up is formed in the surrounding gas, enclosed in the PA cell, which is recorded by a microphone (Rosencwaig and Gerscho 1976; Rousset et al. 1983) The detected signal can be associated with optical, thermal and elastic properties of the sample by means of establishing a TMS model which accounts for all described physical processes, with sample properties being represented as model parameters. It is these parameters which are to be obtained from the recorded signal by means of inverse solving, which classifies photoacoustics into model-dependent experimental techniques.

In order to obtain satisfactory level of accuracy in the determination of physical properties, in model-dependent techniques, it is of utter importance to develop an optimal TMS model. Herein, the theoretical model of frequency PA response in a minimum-volume PA cell relates amplitude and phase of the variation of the recorded acoustic signal to two optical properties of the sample (reflection and absorption coefficient) and to four thermoelastic properties (coefficients of thermal diffusion and thermal conduction, linear coefficient of thermal expansion and heat velocity), while in semiconductors there are five additional properties to follow (energy gap, ambipolar diffusion coefficient, lifetime of photo-generated carriers and velocities of surface generation and recombination). Basing the research on PA frequency measurements, up to eleven physical properties of the material can be assessed! However, the listed properties affect PA response in very complex and non-linear manner, and, besides that, each influence is dependent on modulation frequency. In addition, small variations in model parameter values result in large variations of the model solution, meaning that inverse PA problem is non-linear, ill-conditioned problem of mathematical physics (Power 2002). With this in mind, this task needs to be carefully assessed from a multitude of aspects.

The analysis of the model for various materials – metals, semiconductors and polymers – has indicated different physical processes to be dominant in the

experimentally obtainable frequency range. However, in this case, the influence of thermal diffusivity and linear coefficient of thermal expansion are the ones which affect the PA response the most.

In this paper, a SCIP is developed for thermoelastic characterization of semiconductors, based on previous experience in polymer characterization (Nesic et al. 2019; Nesic et al. 2018), with overall good results in a limited measurement frequency range, i.e. in the range where the influence of the measurement chain can be neglected, where only one PA response component is dominant. Besides that, an ANN based procedure is developed, tailored to a limited measurement frequency range, based on previous experience in semiconductor characterization performed in the whole frequency range and on measurements previously preprocessed in order to be deprived of measurement chain influence (Djordjevic et al. 2020b; Djordjevic et al. 2019). Finally, the results of these two approaches are compared. The aim of this research is to discover the methodology inverse PA problem solving with maximum precision, reliability and applicability on various samples and in various transmission PA experiments, with different microphones and other measurement chain elements.

In Chapter 2, the model of semiconductor frequency PA response is presented and its sensitivity to the variations of thermal diffusivity and linear expansion coefficient is discussed. In Chapter 3, both techniques of inverse problem solving are described: the self-consistent procedure and the neural network. In Chapter 4, the results of both techniques are presented and discussed. Finally, in Chapter 5, the most important conclusions are drawn.

2. TMS modeling – direct problem solving

The core of the experimental set-up consists of the light source, a *minimum volume PA cell*, and the microphone (Rabasovic et al. 2009). The light source is either a LED or a laser diode, its power ranging from 0.8 to 8mW and its wavelength being 660nm, intensity-modulated by a driver. This way produced electromagnetic radiation is projected on a sample, which is mounted on a minimum volume PA cell in the manner of a simple supported plate. The cell consists of a microphone and a photodiode, both installed in an Aluminum shield – quite inexpensive concept promising good signal-to-noise ratio (Balderas-Lopez and Mandelis 2001; Perondi and Miranda 1987). The electret microphone diameter (ECM60) is 9.8mm, its sensitivity being 2.5mVPa^{-1} ; the light source is intensity modulated and frequency-dependent measurements of PA response are performed using a lock-in amplifier. A schematic representation of such a transmission configuration is given in Fig 1:

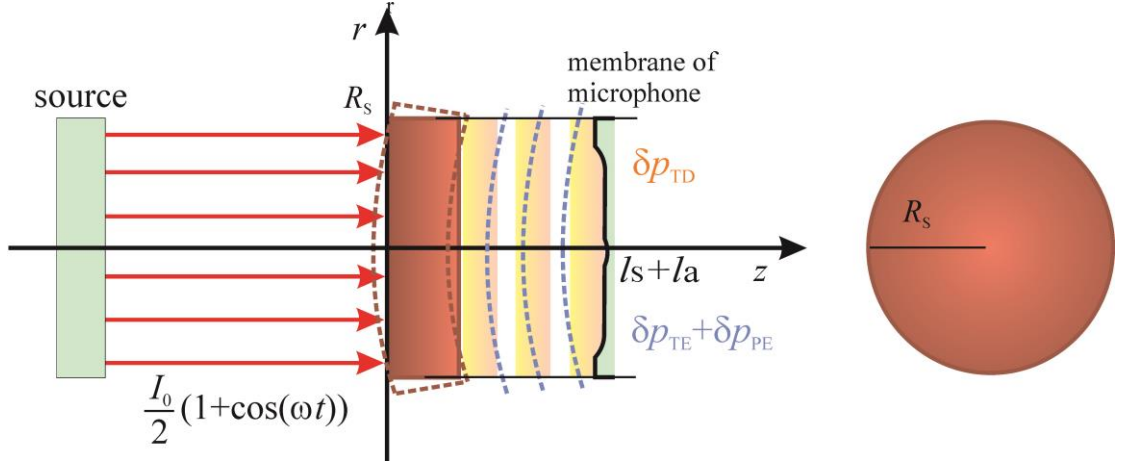


Fig 1 Schematic representations of the geometry of the problem in transmission photoacoustic configuration.

The measured open-cell PA response $\mathcal{S}_{\text{exp}}^{\circ}(f)$ can be represented in the following form:

$$\mathcal{S}_{\text{exp}}^{\circ}(f) = A_{\text{exp}}(f) \exp[i\varphi_{\text{exp}}(f)] = \mathcal{G}(f) \delta \beta_{\text{total}}^{\circ}(f), \quad (1)$$

where $A_{\text{exp}}(f)$ and $\varphi_{\text{exp}}(f)$ are its respective amplitude and phase, i is the complex unit, f is the modulation frequency, $\mathcal{G}(f)$ is the instrumental complex transfer function and $\delta \beta_{\text{total}}^{\circ}(f)$ is the pressure variations signal. To find the sample properties, one has to fit $\mathcal{S}_{\text{exp}}^{\circ}(f)$ to the $\delta \beta_{\text{total}}^{\circ}(f)$ function, determined by the well-known composite piston theoretical model, which, for semiconductors as the n-type Si considered in this work, establishes that (Markushev et al. 2018; Todorović et al. 2014; Todorović et al. 2013):

$$\delta \beta_{\text{total}}^{\circ}(f) = \delta \beta_{\text{TD}}^{\circ}(f) + \delta \beta_{\text{TE}}^{\circ}(f) + \delta \beta_{\text{PE}}^{\circ}(f), \quad (2)$$

where

$$\delta \beta_{\text{TD}}^{\circ}(f) = \frac{\gamma p_0 \sqrt{D_g}}{l T_0 \sqrt{2\pi i f}} \mathcal{G}_s(l), \quad (3)$$

$$\delta \beta_{\text{TE}}^{\circ}(f) = a_r \frac{\gamma p_0}{V_0} \frac{3\pi R_s^4}{l^3} \int_0^l (x - \frac{l}{2}) \mathcal{G}_s(x) dx, \quad (4)$$

and

$$\delta \beta_{\text{PE}}^{\circ}(f) = d_n \frac{\gamma p_0}{V_0} \frac{3\pi R_s^4}{l^3} \int_0^l (x - \frac{l}{2}) \delta \mathcal{H}_p^{\circ}(x) dx, \quad (5)$$

are thermal-diffusion $\delta \beta_{TD}^c(f)$, thermoelastic $\delta \beta_{TE}^c(f)$ and plasmaelastic $\delta \beta_{PE}^c(f)$ components of the PA signal. Here, γ is the adiabatic ratio, T_0 and p_0 are the ambient temperature and pressure, respectively, V_0 and l_c are the PA cell volume and its length, l is the sample thickness, R_s is the radius of the sample D_g is thermal diffusivity of the gas in the PA cell, d_n is the coefficient of electronic deformation, and $\delta \mathcal{H}_\rho^c$ and \mathcal{V}_ρ^c are complex representatives of the density of photogenerated excess charge carriers and of the temperature variations, respectively.

The complex representative of the dynamic component of the photo-generated minority carrier density across the sample $\delta \mathcal{H}_\rho^c(x)$ is given by:

$$\delta \mathcal{H}_\rho^c(x) = \mathcal{A}_+^c e^{-x/l^c} + \mathcal{A}_-^c e^{-x/l^c} - A e^{-\beta x}, \quad (6)$$

where $A = \beta I_0 / (\varepsilon D_p (\beta^2 - \mathcal{L}^c))$, $\mathcal{L}^c = L_p / \sqrt{(1+i\omega\tau)}$, and where $L_p = \sqrt{D_p \tau}$ is the excess carrier (holes) diffusion length, characterized by their diffusion coefficient D_p and lifetime τ , β is optical absorption coefficient and the integration constants \mathcal{A}_\pm^c are defined by :

$$\mathcal{A}_\pm^c = A \frac{(v_\beta + s_1)(\mathcal{V}_\beta m s_2) e^{m/l^c} - (\mathcal{V}_\beta \pm s_1)(v_\beta - s_2) e^{-\beta l}}{(\mathcal{V}_\beta + s_1)(\mathcal{V}_\beta + s_2) e^{l/l^c} - (\mathcal{V}_\beta - s_1)(\mathcal{V}_\beta - s_2) e^{-l/l^c}}, \quad (7)$$

depending strongly on the relative values of characteristic diffusion velocities $\mathcal{V}_\beta = D_p / \mathcal{L}^c$ and $v_\beta = \beta D_p$, as well as on the velocities of surface generation and recombination on irradiated and back surface, s_1 and s_2 , respectively.

The complex representative of dynamic component of temperature distribution across the sample thickness, due to its periodical heating, $\mathcal{V}_s^c(x)$ is given as:

$$\mathcal{V}_s^c(x) = \mathcal{V}_{\text{term}}^c(x) + \mathcal{V}_{\text{sr}}^c(x) + \mathcal{V}_{\text{br}}^c(x), \quad (8)$$

where thermalization, surface and bulk recombination components are defined as (Markushev et al. 2018):

$$\mathcal{V}_{\text{term}}^c(x) = \frac{I_0}{k} \frac{\varepsilon - \varepsilon_g}{\varepsilon} \frac{\beta}{\beta^2 - \mathcal{C}^c} \left\{ \frac{\mathcal{C}^c \cosh[\mathcal{C}^c(x-l)] - e^{-\beta l} \cosh(\mathcal{C}^c \alpha)}{\sinh(\mathcal{C}^c l)} - e^{-\beta x} \right\}, \quad (9)$$

$$\mathcal{S}_{\text{sr}}^{\mathcal{C}}(x) = \frac{\varepsilon_g s_1 \delta \mathcal{H}_p^{\mathcal{C}}(0) \cosh(\mathcal{C}(x-l)) + s_2 \delta \mathcal{H}_p^{\mathcal{C}}(l) \cosh(\mathcal{C}x)}{k \mathcal{C} \mathcal{E}_0} \sinh(\mathcal{C}b). \quad (10)$$

and

$$\mathcal{S}_{\text{tr}}^{\mathcal{C}}(x) = \frac{\varepsilon_g \mathcal{B}_1^{\mathcal{C}}}{\tau k \mathcal{C} \mathcal{E}_0} \left[\frac{\mathcal{B}_2^{\mathcal{C}} e^{\mathcal{C}x} + \mathcal{B}_3^{\mathcal{C}} e^{-\mathcal{C}x}}{2 \sinh(\mathcal{C}b)} - \frac{1}{\mathcal{E}_0 - 1} \left(\frac{\delta \mathcal{H}_p^{\mathcal{C}}(x)}{\mathcal{B}_1^{\mathcal{C}}} + \frac{\mathcal{E}_0^{\mathcal{C}} - \mathcal{E}_0}{\mathcal{E}_0^{\mathcal{C}} - 1} e^{-\beta x} \right) \right]. \quad (11)$$

Here, I_0 is the flux of light irradiation, ε is the photon energy, ε_g is the energy gap of the semiconductor, k is thermal conductivity of the semiconductor, $\mathcal{E}_0^{\mathcal{C}} = \beta / \mathcal{C}$, $\mathcal{E}_0 = (\mathcal{L} \mathcal{C})^{-1}$, $\mathcal{C} = (1+i)/\mu$ being complex heat diffusion coefficient, $\mu = \sqrt{D_T / \pi f}$ being thermal diffusion length of the semiconductor and D_T being thermal diffusivity, while the integration constants $\mathcal{B}_n^{\mathcal{C}}$ ($n = 1, 2, 3, 4, 5$) are defined as:

$$\mathcal{B}_1^{\mathcal{C}} = -\frac{\beta I_0}{\varepsilon D_p (\beta^2 - \mathcal{E}_0^{\mathcal{C}})},$$

$$\mathcal{B}_2^{\mathcal{C}} = \mathcal{B}_4^{\mathcal{C}} e^{-\mathcal{C}b} + \mathcal{B}_5^{\mathcal{C}},$$

$$\mathcal{B}_3^{\mathcal{C}} = \mathcal{B}_4^{\mathcal{C}} e^{\mathcal{C}b} + \mathcal{B}_5^{\mathcal{C}},$$

and

$$\mathcal{B}_4^{\mathcal{C}} = -\frac{\mathcal{E}_0^{\mathcal{C}}}{\mathcal{E}_0^{\mathcal{C}} - 1} \frac{\frac{1}{\mathcal{B}_1^{\mathcal{C}}} \left[\delta \mathcal{H}_p^{\mathcal{C}}(l) - \delta \mathcal{H}_p^{\mathcal{C}}(0) \cosh(l / \mathcal{L}^{\mathcal{C}}) \right] - \cosh(l / \mathcal{L}^{\mathcal{C}}) + e^{-\beta l}}{\sinh(l / \mathcal{L}^{\mathcal{C}}) \cdot (\mathcal{E}_0^{\mathcal{C}} - 1)} - \frac{\mathcal{E}_0^{\mathcal{C}}}{\mathcal{E}_0^{\mathcal{C}} - 1},$$

$$\mathcal{B}_5^{\mathcal{C}} = \frac{\mathcal{E}_0^{\mathcal{C}}}{\mathcal{E}_0^{\mathcal{C}} - 1} \frac{\frac{1}{\mathcal{B}_1^{\mathcal{C}}} \left[\delta \mathcal{H}_p^{\mathcal{C}}(l) \cosh(l / \mathcal{L}^{\mathcal{C}}) - \delta \mathcal{H}_p^{\mathcal{C}}(0) \right] - 1 + e^{-\beta l} \cosh(l / \mathcal{L}^{\mathcal{C}})}{\sinh(l / \mathcal{L}^{\mathcal{C}}) \cdot (\mathcal{E}_0^{\mathcal{C}} - 1)} + \frac{\mathcal{E}_0^{\mathcal{C}} e^{-\beta l}}{\mathcal{E}_0^{\mathcal{C}} - 1}.$$

According to Eqs. (1)-(11), the adjustment of $\mathcal{S}_{\text{exp}}^{\mathcal{C}}(f)$ to $\delta \mathcal{H}_{\text{total}}^{\mathcal{C}}(f)$ can lead to the determination of the sample properties, such as thermal diffusivity D_T , the coefficient of thermal expansion a_T , etc.

In Fig. 2, amplitude and phase data of PA response of Silicon are presented (experiment and theory):

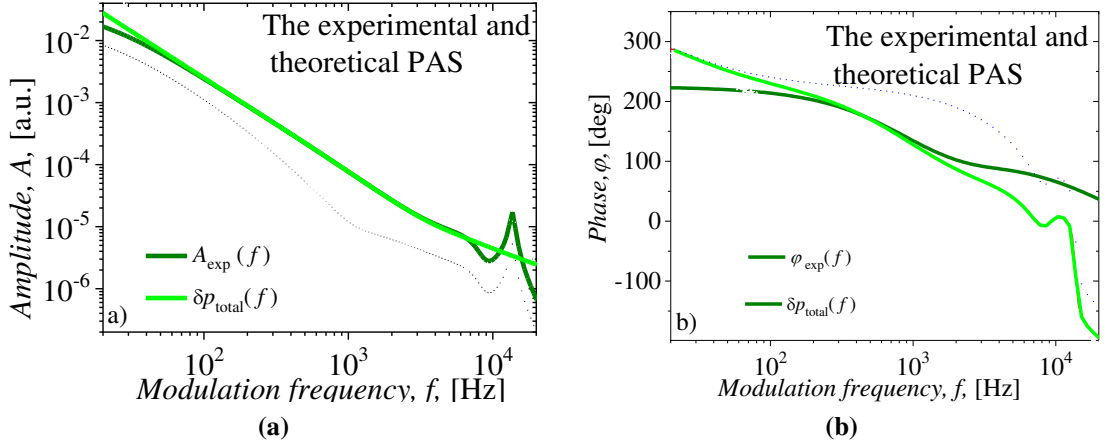


Figure 2(a) Amplitude and (b) phase of the measured $S_{\text{exp}}^{\%}(f)$ (green) and calculated PA response $\delta p_{\text{PE}}(f)$ (light green) as the functions of modulation frequency f (Djordjevic et al. 2020a)

Comparing the prediction of the abovementioned model to the experimental measurements on 150 μm thick Silicon sample, it is shown that TMS model matches the experiment only in the (50Hz – 2kHz) frequency range. Notable difference at low and at high frequencies is attributed to the influence of the noise and to the influence of the measurement chain, so the utilization of the whole frequency measurement range demands detailed analysis and the elimination of these influences (Djordjevic et al. 2020a; Jordovic-Pavlovic et al. 2020; Markushev et al. 2020; Pavlović et al. 2019). In this paper, inverse solving procedures are developed on a limited frequency range, aiming at the determination of silicon properties with dominant influence in the mentioned range, namely the coefficient of thermal diffusion and linear thermal expansion coefficient. Literature values of used parameters are, among others, given in Table 1.

Table 1 Parameters, constants

	labels	values
Adiabatic index for air	γ	1.4
Standard pressure	$p_0[\text{Pa}]$	10^5
Standard temperature	$T_0[\text{K}]$	300
Light irradiation flux	$I_0[\text{Wm}^{-2}]$	10
Coefficient of thermal diffusion of Si	$D_T[\text{m}^2\text{s}^{-1}]$	$(8.1-9.9)\times 10^{-5}$
Linear thermal expansion coefficient	$\alpha_T[\text{K}^{-1}]$,	$(2.34-2.86)\times 10^{-6}$
Thermal conductivity of Si	$k[\text{Wm}^{-1}\text{K}^{-1}]$	150.0
Minority carriers thermal diffusivity	$D_p[\text{m}^2\text{s}^{-1}]$	1.2×10^{-3}
Minority carriers diffusion length	$L_p[\text{m}]$	77.46×10^{-6}
Minority carriers lifetime	$\tau[\text{s}]$	5×10^{-6}
Recombination velocity of the front surface	$s_1[\text{ms}^{-1}]$	2
Recombination velocity of the rear surface	$s_2 [\text{ms}^{-1}]$	24
Coefficient of electronic deformation	$d_n[\text{m}^3]$	-9×10^{-31}

Optical absorption	$\beta[\text{m}^{-1}]$	2.58×10^5
Coefficient of thermal diffusion of air	$D_g[\text{m}^2\text{s}^{-1}]$	2.0566×10^{-5}
Sample radius	$R_s[\text{m}]$	4×10^{-3}
FA cell radius	$R_c[\text{m}]$	3.65×10^{-3}
FA cell length	$l_c[\text{m}]$	1×10^{-3}
Photon energy	$\varepsilon[\text{J}]$	3.01×10^{-19}
Energy gap	$\varepsilon_g[\text{J}]$	1.78×10^{-19}
Optical reflectivity	$R[\text{m}^{-1}]$	0.35

As can be seen in Fig. 2a, the amplitude of PA response in the range (50-2000Hz) changes several orders of magnitude of its value. In order to eliminate insufficiently known optical excitation and amplification influences, signal normalization at a thinner sample of the same kind, previously well characterized, is introduced (Balderas-Lopez and Mandelis 2003).

In Fig. 3, normalized amplitude and phase data is presented for the $D_T \pm 0.1D_T$ of thermal diffusivity change, where $D_T=9 \times 10^{-5} \text{ m}^2\text{s}^{-1}$.

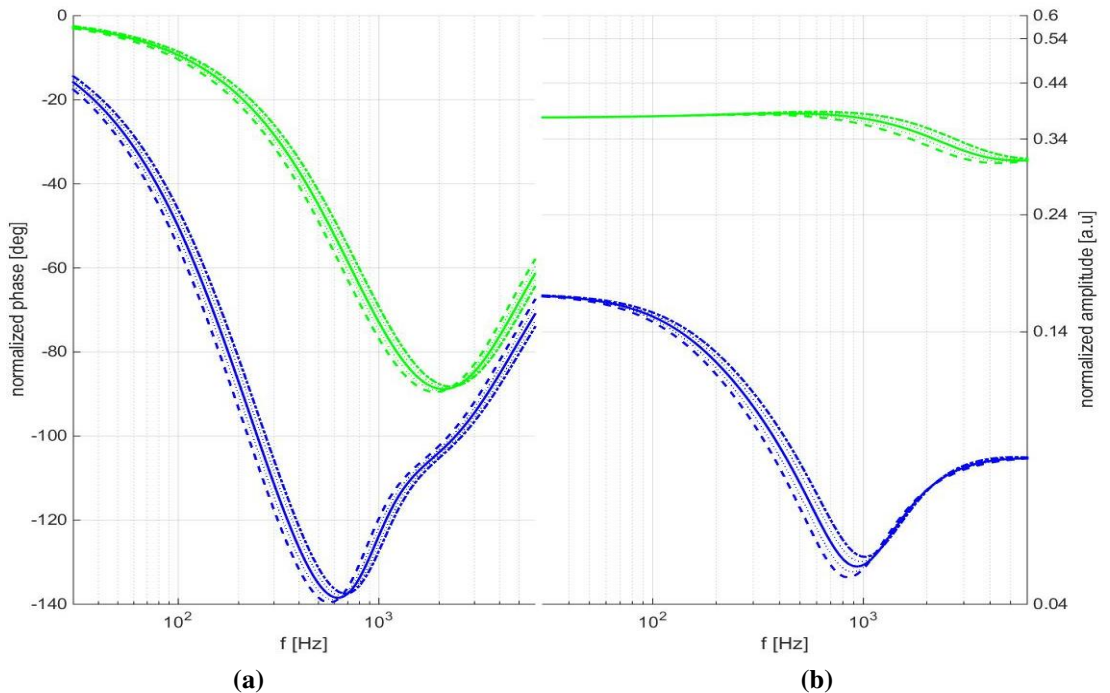


Figure 3 Phase (a) and amplitude (b) of the PA response of Si samples at 900 μm (blue lines) and 400 μm (green lines), normalized on PA response at 150 μm , for $a_T=2.6 \times 10^{-6} \text{ K}^{-1}$ and for variation of D_T in literature range given in Table 1. The dashed lines, full lines and dash-dot lines correspond to $D_T=8.1 \times 10^{-5} \text{ m}^2\text{s}^{-1}$, $D_T=9 \times 10^{-5} \text{ m}^2\text{s}^{-1}$, and $D_T=9.9 \times 10^{-5} \text{ m}^2\text{s}^{-1}$, respectively.

In Fig. 4, normalized amplitude and phase data is presented for the $a_T \pm 0.1a_T$ of linear thermal expansion coefficient change, where $a_T=2.6 \times 10^{-6} \text{ K}^{-1}$.

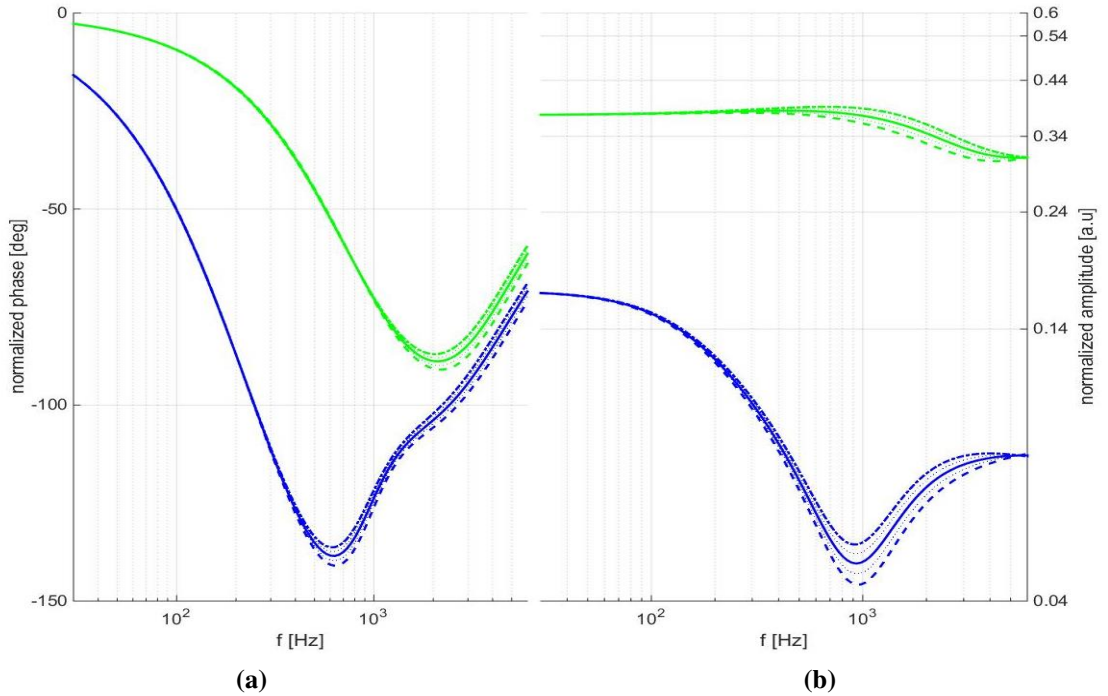


Figure 4 Phase (a) and amplitude (b) of the PA response of Si samples at 900µm (blue lines) and 400µm (green lines), normalized on PA response at 150µm, for $D_T=9 \times 10^{-5} \text{ m}^2\text{s}^{-1}$ and for variation of a_T in literature range given in Table 1. The dashed lines, full lines and dash-dot lines correspond to $a_T=2.34 \times 10^{-6} \text{ K}^{-1}$, $a_T=2.6 \times 10^{-6} \text{ K}^{-1}$, and $a_T=2.86 \times 10^{-6} \text{ K}^{-1}$, respectively.

As can be seen from Fig. 3, thermal diffusivity affects both amplitude and phase characteristics of PA response in the whole frequency range. The influence of the coefficient of thermal expansion is more noticeable in amplitude characteristics and at high frequencies, as can be observed in Fig. 4. Contrary to the case with polymers, where the dominance of the PA component (Eq.4) in the observed frequency range results in linear coefficient of thermal expansion not affecting the normalized PA response, in the case of semiconductors, in this frequency range, this influence is visible, especially in amplitude characteristics.

3. Inverse procedures

3.1 Self-Consistent Inverse Procedure – SCIP

Analytical considerations of the model revealed that the phase of the PA response exhibits stronger dependence upon the parameter of thermal diffusivity, D_T , and thus it can be estimated only from this part of the PA response with satisfactory accuracy. After the estimation, D_T is put into the expression for the amplitude response thus improving the reliability of fitting the coefficient of thermal expansion.

In brief, the SCIP consists of two iterative single-parameter fitting processes: the first one aimed at thermal diffusivity determination and the second one, concerning the estimation of linear coefficient of thermal expansion (see Fig5).

In each iterative process, the parameter value is taken from its literature range and it is varied by the addition (or the subtraction) of 0.1% of its initial value, calculating the

corresponding PA response in each iteration and comparing it to the corresponding PA response of the numerical experiment. The numerical experiment is obtained by the calculation of amplitude and phase characteristics in the limited frequency range (ROI) from 50 Hz to 2 kHz (Fig. 2) with preset values of D_T and a_T randomly taken from the corresponding literature range, given in Table 1. The calculated values are normalized to amplitude and phase characteristics of a well characterized 150 μm thick semiconductor sample ($D_T = 9.0 \times 10^{-5} \text{m}^2 \text{s}^{-1}$ and $a_T = 2.6 \times 10^{-6} \text{K}^{-1}$). The comparison method is based on simple MSE computation scaled on the ROI. These iterations are repeated until one of the conditions is met: either a satisfactory match is achieved between the mentioned preset PA response and the calculated one (i.e. minimum value of the SME on the observed ROI), or the literature range boundary value is reached (security check). Then, the parameter value from the ongoing iteration is recorded as the closest one to the value corresponding to the preset PA response and it is considered the SCIP result. At the same time, the relative error for each parameter is calculated (in percentage), i.e. as the difference of value obtained by the SCIP iterations and the correct (i.e. preset) value, divided by the preset value. These error values represent the characteristic of the SCIP.

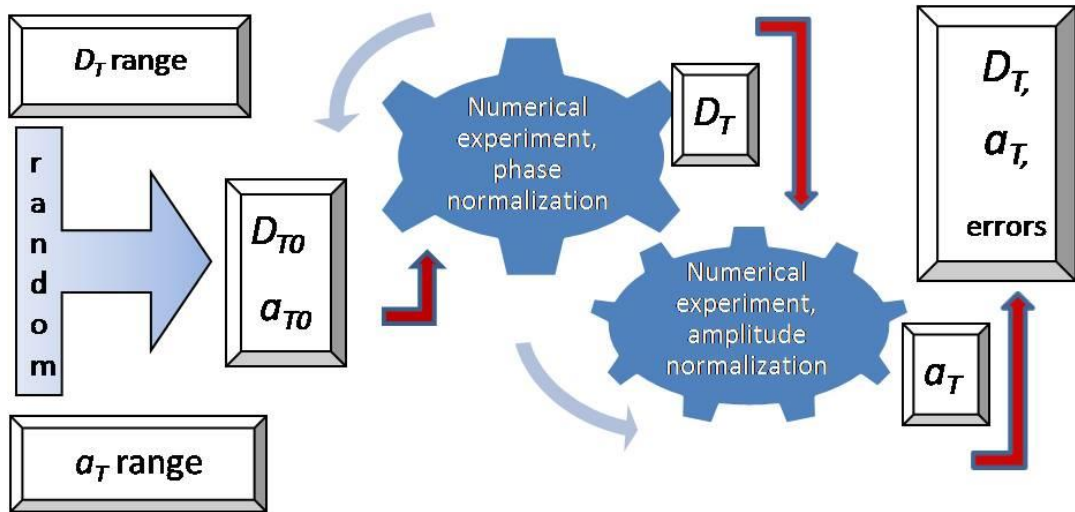


Figure 5 SCIP - schematic diagram

The self-consistency of the inverse procedure is reflected in the fact that, firstly, D_T is extracted from the phase data of the PA response, and, secondly, this result is utilized in the calculation process of the determination of a_T from the amplitude data of the PA response.

3.2 SCIP results

In Fig6, the results of the SCIP after thirty numerical experiments are presented. The results are sorted in ascending order of preset D_T (Fig. 6, up) and preset a_T (Fig. 6, down). The preset values are presented in red. Alongside, corresponding estimates are presented in green (400 μm thick silicon PA response normalized on the PA response at 150 μm) and in blue (900 μm thick silicon PA response normalized on the PA response at 150 μm).

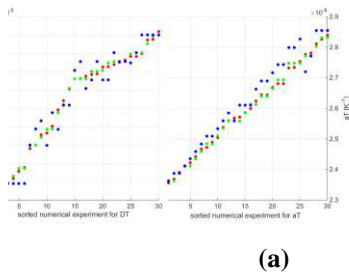


Figure 6 The estimated values of a) D_T and b) a_T for 30 numerical experiments, sorted in ascending order of preset D_T and a_T for two levels of sample thickness. The preset values of D_T and a_T for each experiment are presented by red dots. Corresponding estimates are presented in green dots (400 μm thick silicon PA response normalized on the PA response at 150 μm) and in blue dots (900 μm thick silicon PA response normalized on the PA response at 150 μm).

As can be noted in Fig. 6a, the estimated values of D_T in the case of 400/150 normalization (green dots) are closer to the expected values of the numerical experiment (red dots, sorted in ascending order) in comparison to the ones based on 900/150 normalization (blue dots). With regard to theoretical considerations, presented in Fig3, this result seem to be unexpected, since normalized phase difference is lower in thinner samples (Fig4b), and the accuracy of D_T results is expected to be lower in thinner samples.

In Fig6b the accuracy of a_T estimates is also better in thinner samples. This result is also unexpected, based on theoretical considerations presented in Fig5, since the difference in normalized amplitudes is larger in thick samples (Fig4b).

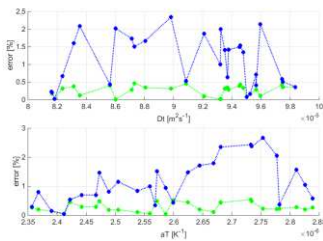


Figure 7 Relative errors of D_T (up) and a_T (down) obtained by the SCIP as the function of the corresponding parameter value preset by numerical experimental

In Fig7 relative estimation errors gained in numerical experiments are presented as the function of preset D_T (up) and a_T (down) values, sorted in ascending order, where green lines are indicative of 400/150 normalization, while blue lines are for the 900/150 one. It can be noted that relative errors of the procedure do not exert any strong dependency on the preset D_T and a_T values, although slight increase is observed in a_T relative error for high values of preset a_T , (blue line in Fig7b).

Maximum and mean values of relative error, regarded as the characteristics of the SCIP and gained after the performance of 30 numerical experiments, are presented in Table2.

Table 2 SCIP results

	Max relative error [%]		Mean relative error [%]	
	D_T	a_T	D_T	a_T
SCIP(400/150)	0.47	0.54	0.27	0.28
SCIP(900/150)	2.34	2.67	1.09	1.21

The analysis of Table 2 shows that maximum as well as mean values of relative error are lower for both D_T and a_T presets in thinner samples (below 1%), while the increase of sample thickness brings these values to around 2.5%. Also, the corresponding error values are lower in the case of D_T in comparison to the case of a_T estimation, i.e. the developed procedure estimates D_T with greater precision than a_T .

3.3 Inverse solution of photoacoustic problem by neural networks

Solving the inverse problem of photoacoustics in frequency domain using some normalization procedure still attracts considerable interest. Especially for the silicon samples of n-type which have the widest industrial application. That is why the necessity to find the procedure of quick and precise experimental determination of silicon individual properties applying some normalization procedure is an ultimate goal which can be achieved, besides the other, by using the artificial neural networks (ANN).

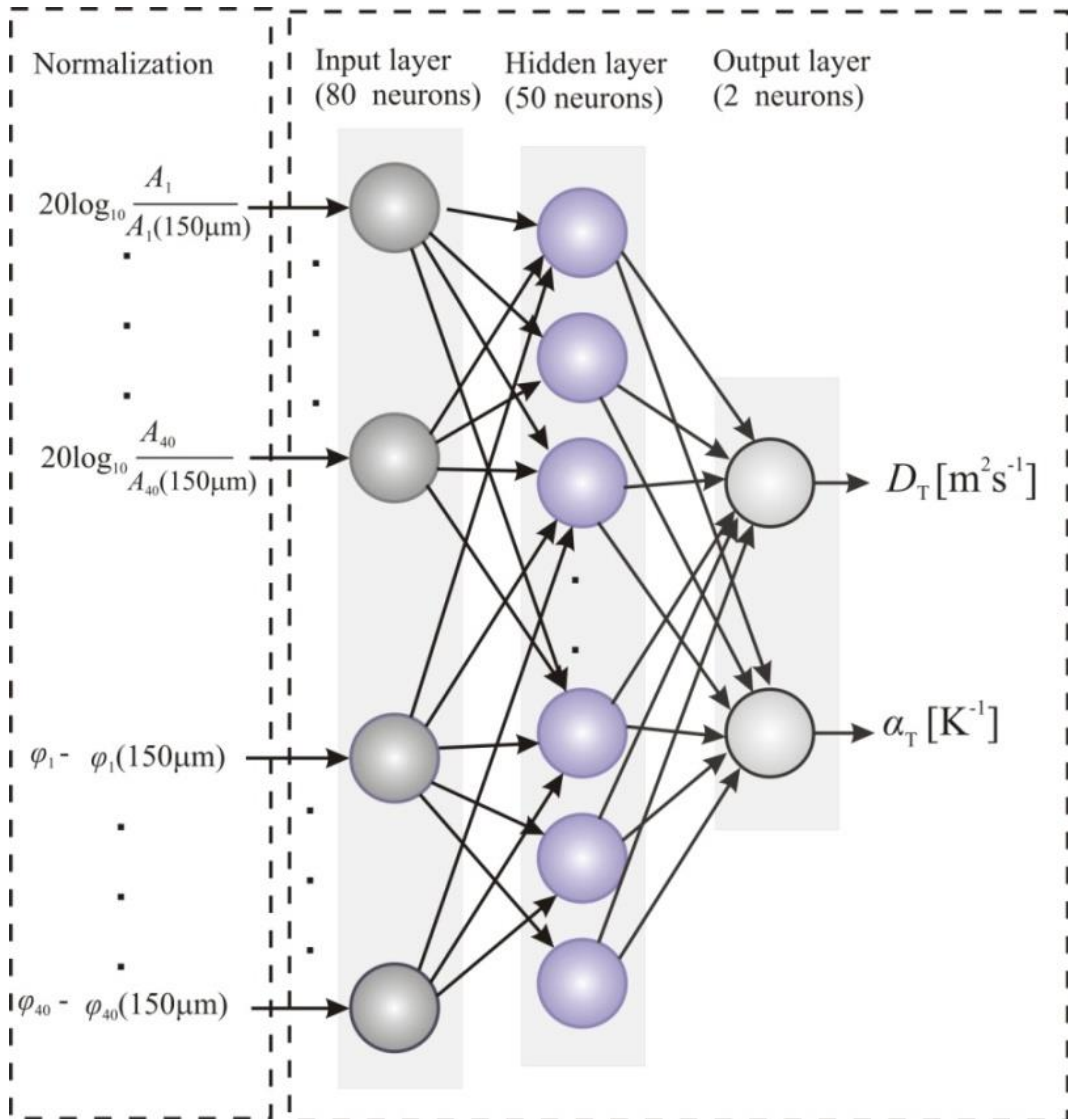


Figure 8 Neural network structure for inverse solution of photoacoustic problem for thermal diffusivity and expansion (2 output layer neurons) with normalized amplitude-phase signals (80 input layer neurons)

Using regression as a supervised learning technique with simple structured ANN one can solve the inverse problem estimating typical semiconductor parameters from the normalized photoacoustic signals as predicted output values of the network (for example, thermal diffusivity, thermal expansion, thickness, etc).

Here, neural networks of the simple structure were formed with one input, one hidden and one output layer, represented in Figure 8. The data used in the input layer are the amplitude-phase characteristics of the normalized photoacoustic signal magnitude defined with 40 modulation frequency values each, so 80 neurons establish the input layer. The output layer consists of two neurons, corresponding to the sample thermal parameters each, thermal diffusivity D_T and thermal expansion α_T . The hidden layer is formed by 50 neurons.

Neural networks presented here are trained in the specific modulation frequency range from 50 Hz to 2 kHz, using a large base of 284 theoretical photoacoustic signals obtained with Equations (2-5) for sample thicknesses of 400 μm and 900 μm , changing the thermal diffusivity and thermal expansion values within the range of $D_T = (8.1-9.9) \times 10^{-5} \text{ m}^2 \text{ s}^{-1}$ and $\alpha_T = (2.34-2.86) \times 10^{-6} \text{ K}^{-1}$, respectively.

The amplitudes of the input signals are normalized with the function $20 \log(A_i / A_i(150 \mu\text{m}))$, $i = 1, 2, 3 \dots, 40$. In such a way their values are reduced to the values that correspond to the changes of the phase, taking the amplitude of 150 μm thick sample as a referent one with constant $D_T = 9.0 \times 10^{-5} \text{ m}^2 \text{ s}^{-1}$ and $\alpha_T = 2.6 \times 10^{-6} \text{ K}^{-1}$. Phases are normalized with the function $\varphi_i - \varphi_i(150 \mu\text{m})$, $i = 1, 2, 3 \dots, 40$, taking the same referent sample thickness.

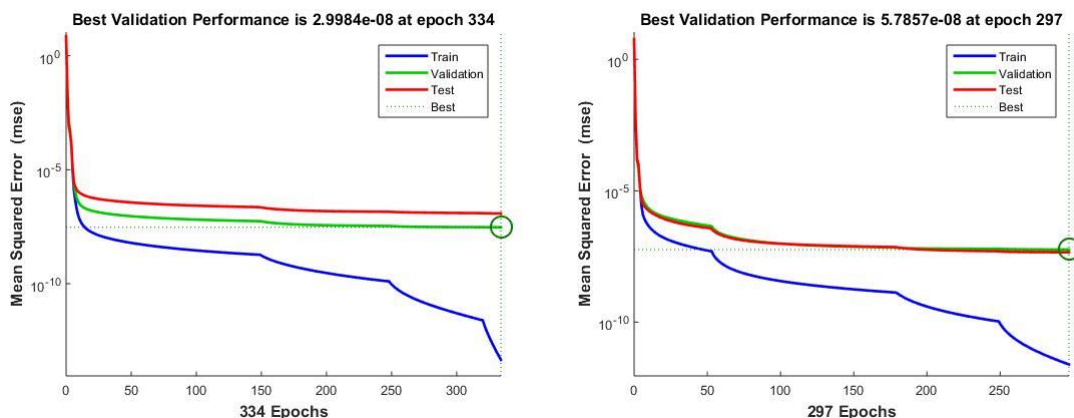


Fig. 9. Training the neural network on two different bases with sample thickness of: a) 400 μm and b) 900 μm normalized with sample thickness of 150 μm .

The results of the network training using back propagation method for both levels of sample thickness of 400 μm and 900 μm normalized with 150 μm sample thickness are shown in Figure 9. The first neural network ANN(400/150) was trained in 297 epochs activating the termination criteria with the performance of $5.7857 \cdot 10^{-8}$

(Figure 9a). The second neural network ANN(900/150) was trained in 334 epochs activating the termination criteria with the performance of $2.9984 \cdot 10^{-8}$ (Figure 9b).

3.4 Results of the neural network predictions

The results of the independent test with 5 signals from the large base, which are not used in network training, were presented for both networks in the Table 3a and 3b, with % relative prediction error (maximum and mean) obtained as a difference between PA signal parameters D_T and a_T and their ANN prediction.

Table 3a. The results of ANN(400/150) prediction based on 5 independent signals taken from the large signal base, not used in network training.

Preset parameters		ANN(400/150) prediction	
$D_T [10^{-5} \text{ m}^2 \text{ s}^{-1}]$	$a_T [10^{-6} \text{ K}^{-1}]$	$D_T [10^{-5} \text{ m}^2 \text{ s}^{-1}]$	$a_T [10^{-6} \text{ K}^{-1}]$
9.9000	2.7950	9.9008	2.7951
9.5625	2.8275	9.5631	2.8275
9.2250	2.8600	9.2252	2.8600
9.0000	2.3400	8.9998	2.3403
8.6625	2.3725	8.6626	2.3722

Table 3b. The results of ANN(900/150) prediction based on 5 independent signals taken from the large signal base, not used in network training.

Preset parameters		ANN(900/150) prediction	
$D_T [10^{-5} \text{ m}^2 \text{ s}^{-1}]$	$a_T [10^{-6} \text{ K}^{-1}]$	$D_T [10^{-5} \text{ m}^2 \text{ s}^{-1}]$	$a_T [10^{-6} \text{ K}^{-1}]$
9.6750	2.6000	9.6748	2.5998
9.3375	2.6325	9.3374	2.6325
9.0000	2.6650	8.9999	2.6648
8.6625	2.6975	8.6630	2.6975
8.3250	2.7300	8.3242	2.7297

Table 4. ANN errors of the ANN(400/150) and ANN(900/150) prediction results in the training step of the networks.

parameters	(%) Max Relative Error		Mean (%) Relative Error	
	D_T	a_T	D_T	a_T
ANN(400/150)	0.0083	0.0128	0.0038	0.0055
ANN(900/150)	0.0099	0.0101	0.0040	0.0052

The results presented in Tables 3a and 3b indicate high network accuracy in the predictions of the sample parameters. Table 4 shows that the errors are much lower than 0,1%, but even that is enough to confirm the theoretical model of photoacoustics used for their training. Namely, the errors for D_T are lower than the errors for a_T in both cases. Also, the errors for D_T decrease while the errors for a_T increase with

decreasing thickness. This is in accordance with the theoretical model of photoacoustics (Equations 2-5) which predicts the dominance of thermal diffusion component of the signal (used to determine D_T) for thinner samples in the entire (50 – 2000) Hz frequency range (other signal components are negligible).

4. Discussion and comparison of SCIP and ANN results

The characteristics of the two presented procedures aimed at inverse solving of PA problem and the estimation of two unknown semiconductor properties, in the frequency range limited to the part where measurement chain influence can be neglected, are described by maximum and mean relative error values, given in Tables 2 and 4. From these tables, it is clearly visible that ANN based procedure is characterized by a hundred (100) times lower level of error. This result can be explained by the fact that certain approximations, introduced in the SCIP in order to lower its processing time and based on previous theoretical considerations, are rough and seem to introduce significant level of error. The most illustrative one is the assumption that the influence of a_T on phase characteristics can be neglected, since it is barely noticeable and present at high frequencies only. This approximation increases the error in a_T estimation by considering that D_T is estimated accurately enough in the first iterative process of the SCIP.

Another difference in methodology between these procedures is the fact that SCIP processes amplitude and phase data separately, while ANN-based procedure processes them simultaneously, effectively discovering (D_T , a_T) pairs which result in the most similar PA response amplitude and phase at the same time.

5. Conclusions

The determination of two or more material properties from a single PA response measurement represents an important problem, the solving of which should result in a broader application of photoacoustics in various areas of science and technology. In this paper, two procedures aimed at solving this kind of problem are presented. Characterization parameters, namely maximum and mean determination relative error, are also proposed.

SCIP is characterized by error values lower than 3%, making this approach a satisfactory choice in the case of rough estimation of D_T and a_T measured properties.

ANN approach is characterized by error values under 0,1%. The result this good establishes it as the method of choice in very accurate D_T and a_T determination from PA measurements, especially in the case where the properties obtained this way are used in further sample characterization, allowing accompanying procedures to bring in their determination errors and still keeping the obtained result within 1% uncertainty boundary.

The comparison of the presented procedures in terms of maximum relative error criterion shows that ANN based methodology is significantly better than the SCIP.

The differences in methodologies are discussed and possible causes of significant errors in the SCIP are reported.

In future explorations, the developed and presented ANN-based procedure can be used as reference method in inverse solving of the PA problem while the SCIP can and should be modified in order to significantly lower the level of relative error.

Declarations

All manuscripts must contain the following sections under the heading 'Declarations'.

If any of the sections are not relevant to your manuscript, please include the heading and write 'Not applicable' for that section.

To be used for all articles, including articles with biological applications

Funding – Not applicable

Conflicts of interest/Competing interests – Not applicable

Availability of data and material – Not applicable

Code availability – Not applicable

Authors' contributions – Not applicable

Additional declarations for articles in life science journals that report the results of studies involving humans and/or animals

Ethics approval – Not applicable

Consent to participate – Not applicable

Consent for publication – Not applicable

List of figures' captions

Figure 1 Schematic representations of the geometry of the problem in transmission photoacoustic configuration.

Figure 2 Amplitude and (b) phase of the measured $S_{\text{exp}}^{\%}(f)$ (green) and calculated PA response $\delta\beta_{\text{PE}}^{\%}(f)$ (light green) as the functions of modulation frequency f (Djordjevic et al. 2020a)

Figure 3 Phase (a) and amplitude (b) of the PA response of Si samples at 900 μm (blue lines) and 400 μm (green lines), normalized on PA response at 150 μm , for $a_T=2.6\times 10^{-6}\text{K}^{-1}$ and for variation of D_T in literature range given in Table 1. The dashed lines, full lines and dash-dot lines correspond to $D_T=8.1\times 10^{-5}\text{m}^2\text{s}^{-1}$, $D_T=9\times 10^{-5}\text{m}^2\text{s}^{-1}$, and $D_T=9.9\times 10^{-5}\text{m}^2\text{s}^{-1}$, respectively.

Figure 4 Phase (a) and amplitude (b) of the PA response of Si samples at 900 μm (blue lines) and 400 μm (green lines), normalized on PA response at 150 μm , for $D_T=9\times 10^{-5}\text{m}^2\text{s}^{-1}$ and for variation of a_T in literature range given in Table 1. The dashed lines, full lines and dash-dot lines correspond to $a_T=2.34\times 10^{-6}\text{K}^{-1}$, $a_T=2.6\times 10^{-6}\text{K}^{-1}$, and $a_T=2.86\times 10^{-6}\text{K}^{-1}$, respectively.

Figure 5 SCIP - schematic diagram

Figure 6 The estimated values of a) D_T and b) a_T for 30 numerical experiments, sorted in ascending order of preset D_T and a_T for two levels of sample thickness. The preset values of D_T and a_T for each experiment are presented by red dots. Corresponding estimates are presented in green dots (400 μm thick silicon PA response normalized on the PA response at 150 μm) and in blue dots (900 μm thick silicon PA response normalized on the PA response at 150 μm).

Figure 7 Relative errors of D_T (up) and a_T (down) obtained by the SCIP as the function of the corresponding parameter value preset by numerical experimental

Figure 8 Neural network structure for inverse solution of photoacoustic problem for thermal diffusivity and expansion (2 output layer neurons) with normalized amplitude-phase signals (80 input layer neurons)

Figure 9 Training the neural network on two different bases with sample thickness of: a) 400 μm and b) 900 μm normalized with sample thickness of 150 μm

References

- Balderas-Lopez, J.A., Mandelis, A.: Thermal diffusivity measurements in the photoacoustic open-cell configuration using simple signal normalization techniques. *J. Appl. Phys.* 90, 2273–2279 (2001). <https://doi.org/10.1063/1.1391224>
- Balderas-Lopez, J.A., Mandelis, A.: Self-normalized photothermal technique for accurate thermal diffusivity measurements in thin metal layers. *Rev. Sci. Instrum.* 74, 5219 (2003). <https://doi.org/10.1063/1.1623626>
- Bialkowski, S.E.: *Photothermal Spectroscopy Methods for Chemical Analysis*. John Wiley & Sons, Inc., New York (1996)
- Djordjevic, K.L., Markushev, D.D., Čojbašić, Ž.M., Galović, S.P.: Inverse problem solving in semiconductor photoacoustics by neural networks. *Inverse Probl. Sci. Eng.* 1–15 (2020)(a). <https://doi.org/10.1080/17415977.2020.1787405>
- Djordjevic, K.L., Galovic, S.P., Jordovic-Pavlovic, M.I., Nestic, M. V., Popovic, M.N., Cojbasic, Z.M., Markushev, D.D.: Photoacoustic optical semiconductor characterization based on machine learning and reverse-back procedure. *Opt. Quantum Electron.* 52, 247 (2020)(b). <https://doi.org/10.1007/s11082-020-02373-x>
- Djordjevic, K.L., Markushev, D.D., Čojbašić, Ž.M., Djordjevic, K.L.: Photoacoustic Measurements of the Thermal and Elastic Properties of n-Type Silicon Using Neural Networks. *Silicon.* 12, 1289–1300 (2019). <https://doi.org/10.1007/s12633-019-00213-6>
- Galovic, S.P., Soskic, Z.N., Popovic, M.N., Stojanovic, Z., Cevizovic, D., Stojanovic, Z.: Theory of photoacoustic effect in media with thermal memory. *J. Appl. Phys.* 116, 0–12 (2014). <https://doi.org/10.1063/1.4885458>
- Jordovic-Pavlovic, M.I., Markushev, D.D., Kupusinac, A.D., Djordjevic, K.L., Nestic, M. V., Galovic, S.P., Popovic, M.N.: Deep Neural Network Application in the Phase-Match Calibration of Gas–Microphone Photoacoustics. *Int. J. Thermophys.* 41, 1–10 (2020). <https://doi.org/10.1007/s10765-020-02650-7>
- Mansanares, A.M., Vargas, H., Galembeck, F., Buijs, J., Bicanic, D.: Photoacoustic characterization of a two-layer system. *J. Appl. Phys.* 70, 7046–7050 (1991)
- Markushev, D., Markushev, D., Galovic, S., Aleksic, S., Pantic, D., Todorovic, D.: The surface recombination velocity and bulk lifetime influences on photogenerated excess carrier density and temperature distributions in n-type silicon. *Facta Univ. - Ser. Electron. Energ.* 31, 313–328 (2018). <https://doi.org/10.2298/fuee1802313m>
- Markushev, D.K., Markushev, D.D., Aleksić, S.M., Pantić, D.S., Galović, S.P., Todorović, D.M., Ordóñez-Miranda, J.: Experimental photoacoustic observation of the photogenerated excess carrier influence on the thermoelastic response of n-type silicon. *J. Appl. Phys.* 128, 95103 (2020). <https://doi.org/10.1063/5.0015657>
- Nestic, M., Popovic, M.N., Galovic, S., Nestic, M., Popovic, M.N., Galovic, S.: Developing the Techniques for Solving the Inverse Problem in Photoacoustics. *Atoms.* 7, 24 (2019). <https://doi.org/10.3390/atoms7010024>
- Nestic, M. V., Popovic, M.N., Rabasovic, M., Milicevic, D., Suljovrujic, E., Markushev, D., Stojanovic, Z.: Thermal Diffusivity of High-Density Polyethylene Samples of Different Crystallinity Evaluated by Indirect Transmission Photoacoustics. *Int. J. Thermophys.* 39, (2018). <https://doi.org/10.1007/s10765-017-2345-0>
- Pavlović, M.J., Markushev, D., Popovic, M.N., Galović, S.: Deep Learning in Development of Model- Dependent Diagnostic : Recognition of Detector Characteristics in Measured Responses. In: *Proceedings of 6th International conference on electrical, electronic, and computing engineering (IcETRAN)* (2019)
- Perondi, L.F., Miranda, L.C.M.: Minimal-volume photoacoustic cell measurement of thermal diffusivity: Effect of the thermoelastic sample bending. *J. Appl. Phys.* 62, 2955–2959 (1987)
- Power, J.F.: Inverse problem theory in the optical depth profilometry of thin films. *Rev. Sci. Instrum.* 73, 4057–4141 (2002). <https://doi.org/10.1063/1.1517054>
- Rabasovic, M.D., Nikolic, M.G., Dramicanin, M.D., Franko, M., Markushev, D.D.: Low-cost, portable photoacoustic setup for solid samples. *Meas. Sci. Technol.* 20, 95902 (2009)
- Rosencwaig, A., Gerscho, A.: Theory of the photoacoustic effect with solids. *J. Appl. Phys.* 47, 64–69 (1976)
- Rousset, L., Lepoutre, F., Bertrand, L.: Influence of thermoelastic bending on photoacoustic experiments related to measurements of thermal diffusivity of metals. *J. Appl. Phys.* 54, 2383–2391 (1983)
- Tam, A.A.C.: Applications of photoacoustic sensing techniques. *Rev. Mod. Phys.* 58, 381–431 (1986)
- Todorović, D.M., Nikolic, P.M.: Carrier transport Contribution on Thermoelastic and Electronic Deformation in Semiconductors. In: Mandelis, A. and Hess, P. (eds.) *Progress in Photothermal and Photoacoustic Science and Technology - Semiconductors and Electronic Materials*. pp. 271–315. SPIE Press, Bellingham, Washington, USA (2000)
- Todorović, D.M., Rabasovic, M.D., Markushev, D.D.: Photoacoustic elastic bending in thin film—Substrate system. *J. Appl. Phys.* 114, 213510 (2013). <https://doi.org/10.1063/1.4839835>
- Todorović, D.M., Rabasovic, M.D., Markushev, D.D., Sarajlić, M.: Photoacoustic elastic bending in thin film-substrate system: Experimental determination of the thin film parameters. *J. Appl. Phys.* 116, (2014). <https://doi.org/10.1063/1.4890346>
- Vargas, H., Miranda, L.C.M.: Photoacoustic and related photothermal techniques. *Phys. Rep.* 161, 43–101 (1988). [https://doi.org/10.1016/0370-1573\(88\)90100-7](https://doi.org/10.1016/0370-1573(88)90100-7)

Figures

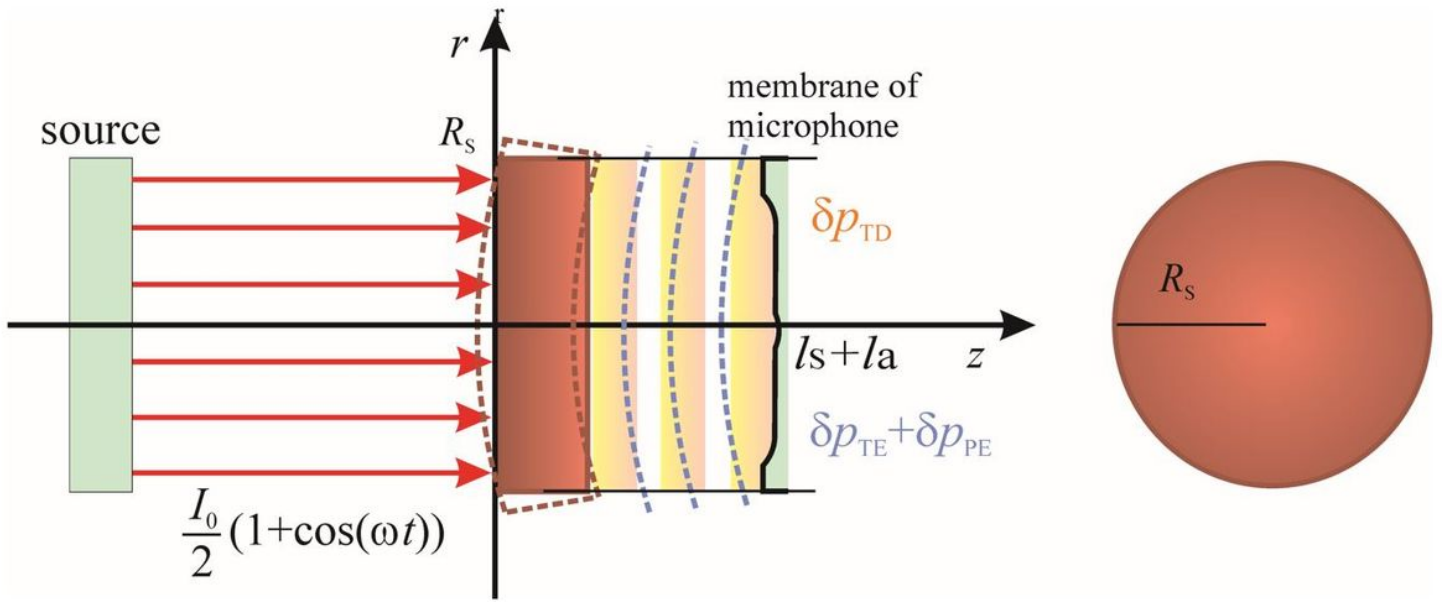


Figure 1

Schematic representations of the geometry of the problem in transmission photoacoustic configuration.

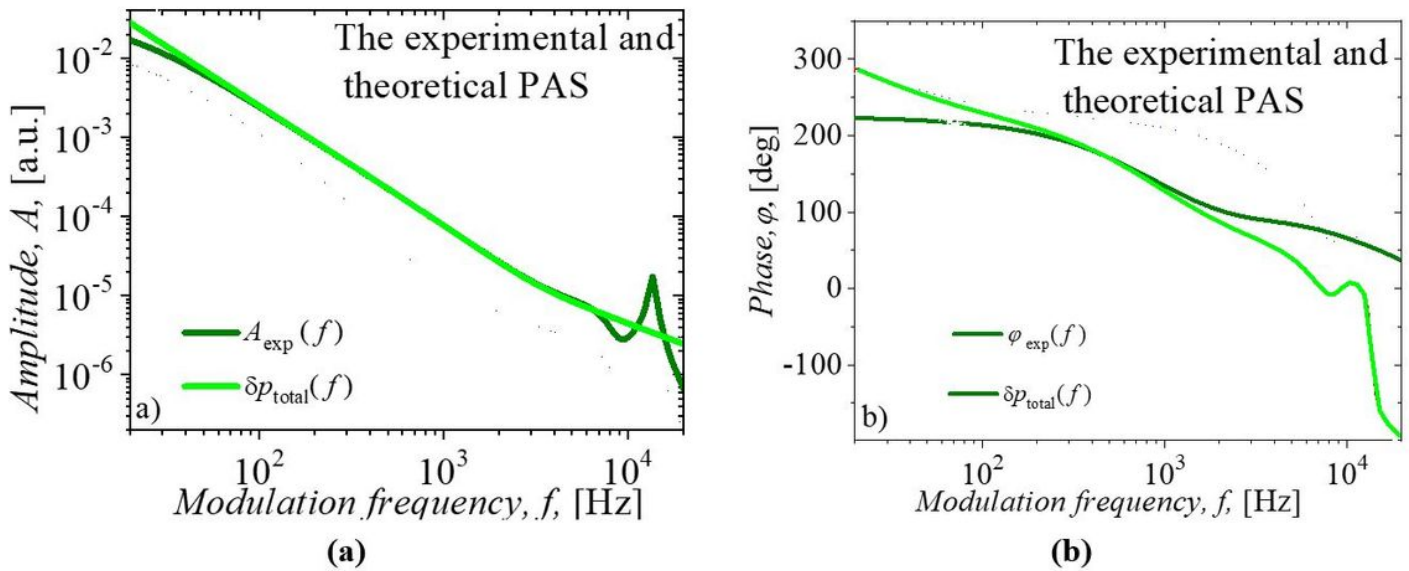


Figure 2

Amplitude and (b) phase of the measured $S_{exp}(f)$ (green) and calculated PA response $\delta p_{PE}(f)$ (light green) as the functions of modulation frequency f (Djordjevic et al. 2020a)

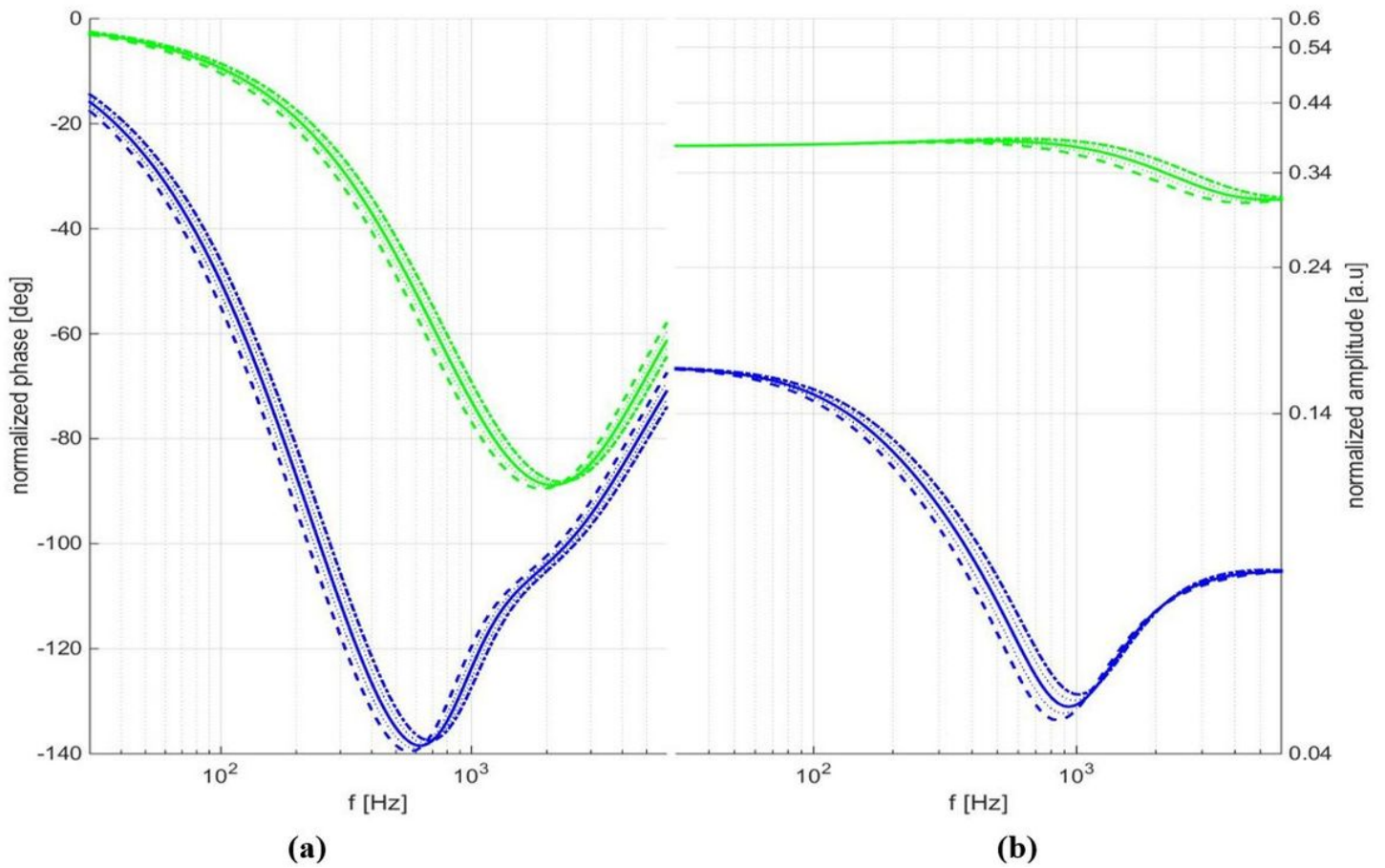


Figure 3

Phase (a) and amplitude (b) of the PA response of Si samples at 900 μm (blue lines) and 400 μm (green lines), normalized on PA response at 150 μm , for $aT = 2.6 \times 10^{-6} \text{ K}^{-1}$ and for variation of DT in literature range given in Table 1. The dashed lines, full lines and dash-dot lines correspond to $DT = 8.1 \times 10^{-5} \text{ m}^2\text{s}^{-1}$, $DT = 9 \times 10^{-5} \text{ m}^2\text{s}^{-1}$, and $DT = 9.9 \times 10^{-5} \text{ m}^2\text{s}^{-1}$, respectively.

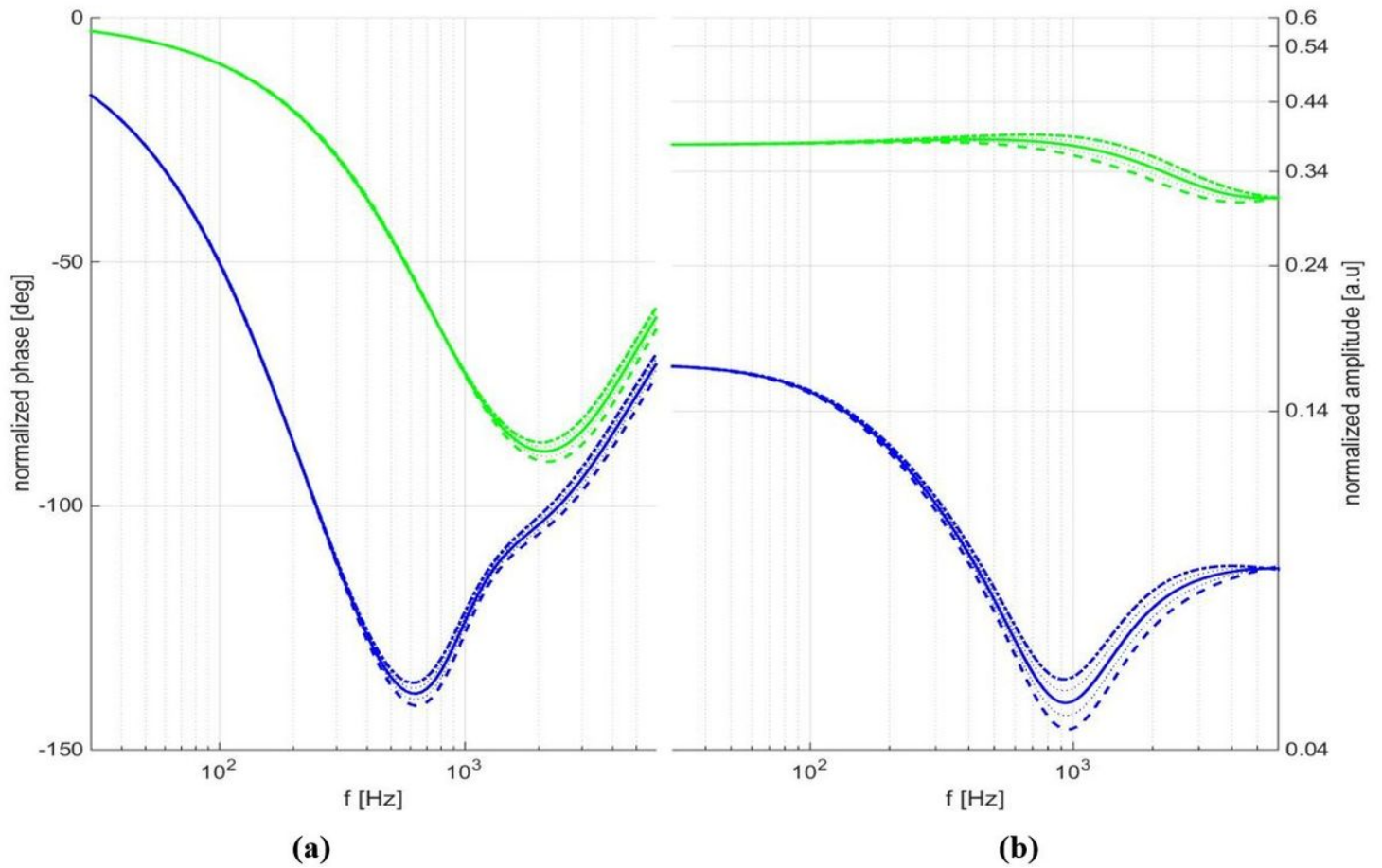


Figure 4

Phase (a) and amplitude (b) of the PA response of Si samples at 900 μm (blue lines) and 400 μm (green lines), normalized on PA response at 150 μm , for $DT=9 \times 10^{-5} \text{ m}^2\text{s}^{-1}$ and for variation of aT in literature range given in Table1. The dashed lines, full lines and dash-dot lines correspond to $aT=2.34 \times 10^{-6} \text{ K}^{-1}$, $aT=2.6 \times 10^{-6} \text{ K}^{-1}$, and $aT=2.86 \times 10^{-6} \text{ K}^{-1}$, respectively.

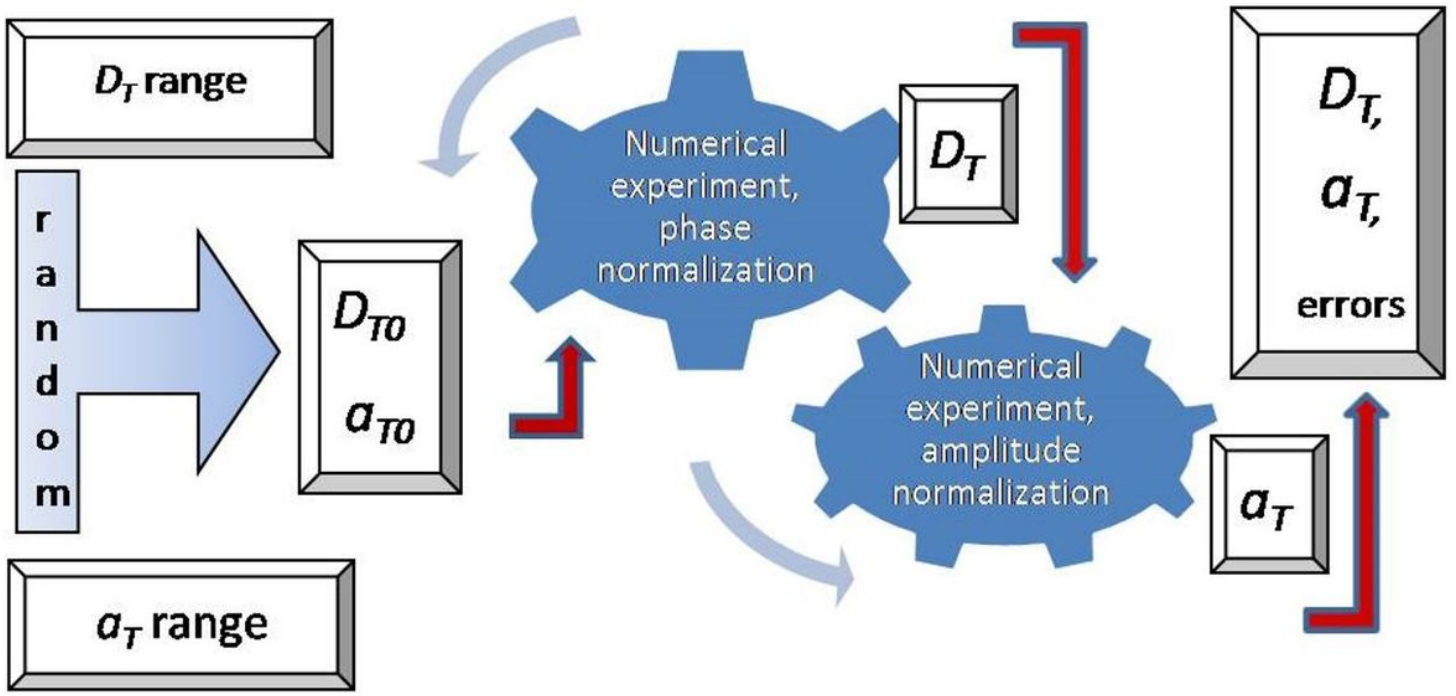


Figure 5

SCIP - schematic diagram

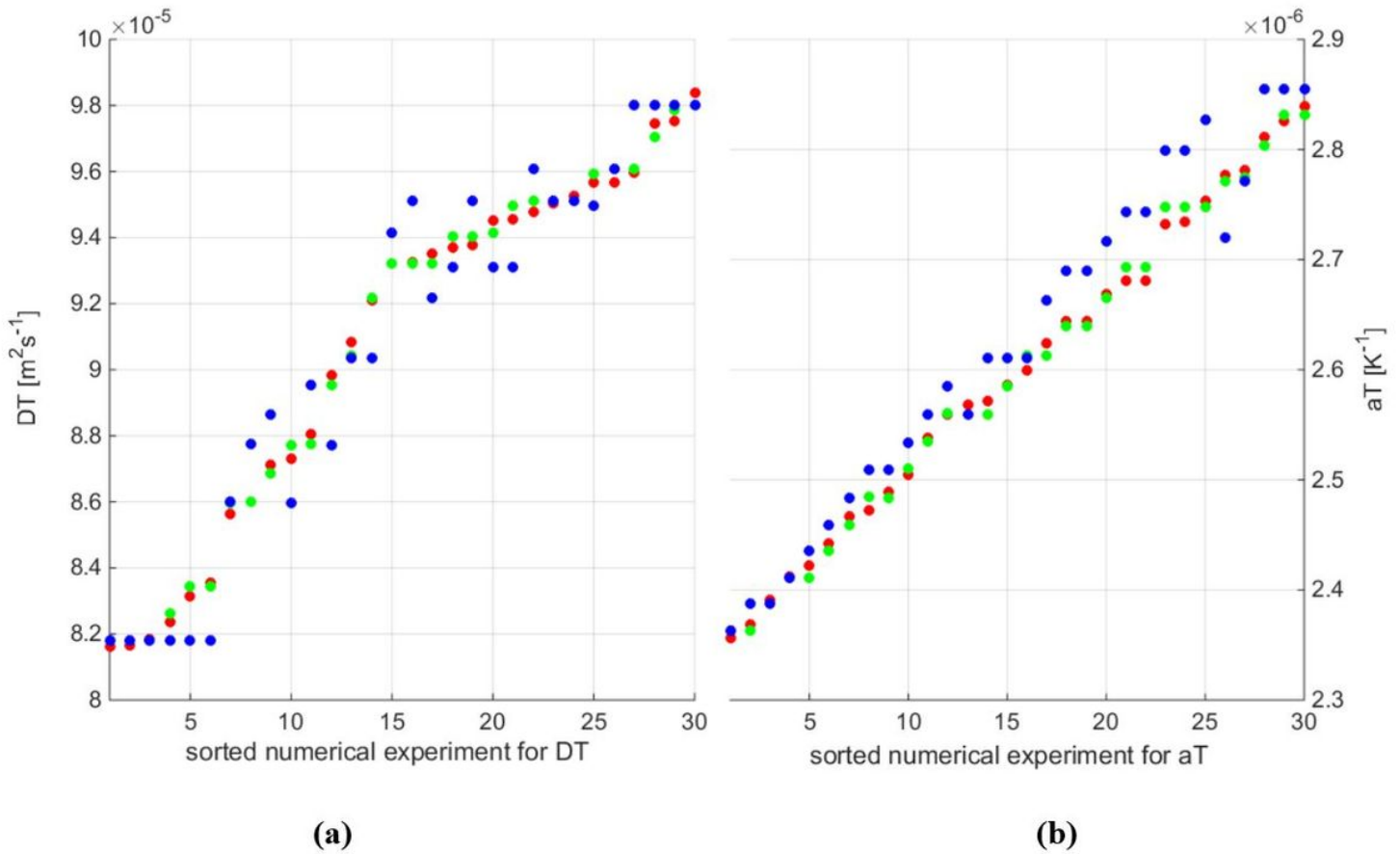


Figure 6

The estimated values of a) DT and b) aT for 30 numerical experiments, sorted in ascending order of preset DT and aT for two levels of sample thickness. The preset values of DT and aT for each experiment are presented by red dots. Corresponding estimates are presented in green dots (400 μm thick silicon PA response normalized on the PA response at 150 μm) and in blue dots (900 μm thick silicon PA response normalized on the PA response at 150 μm).

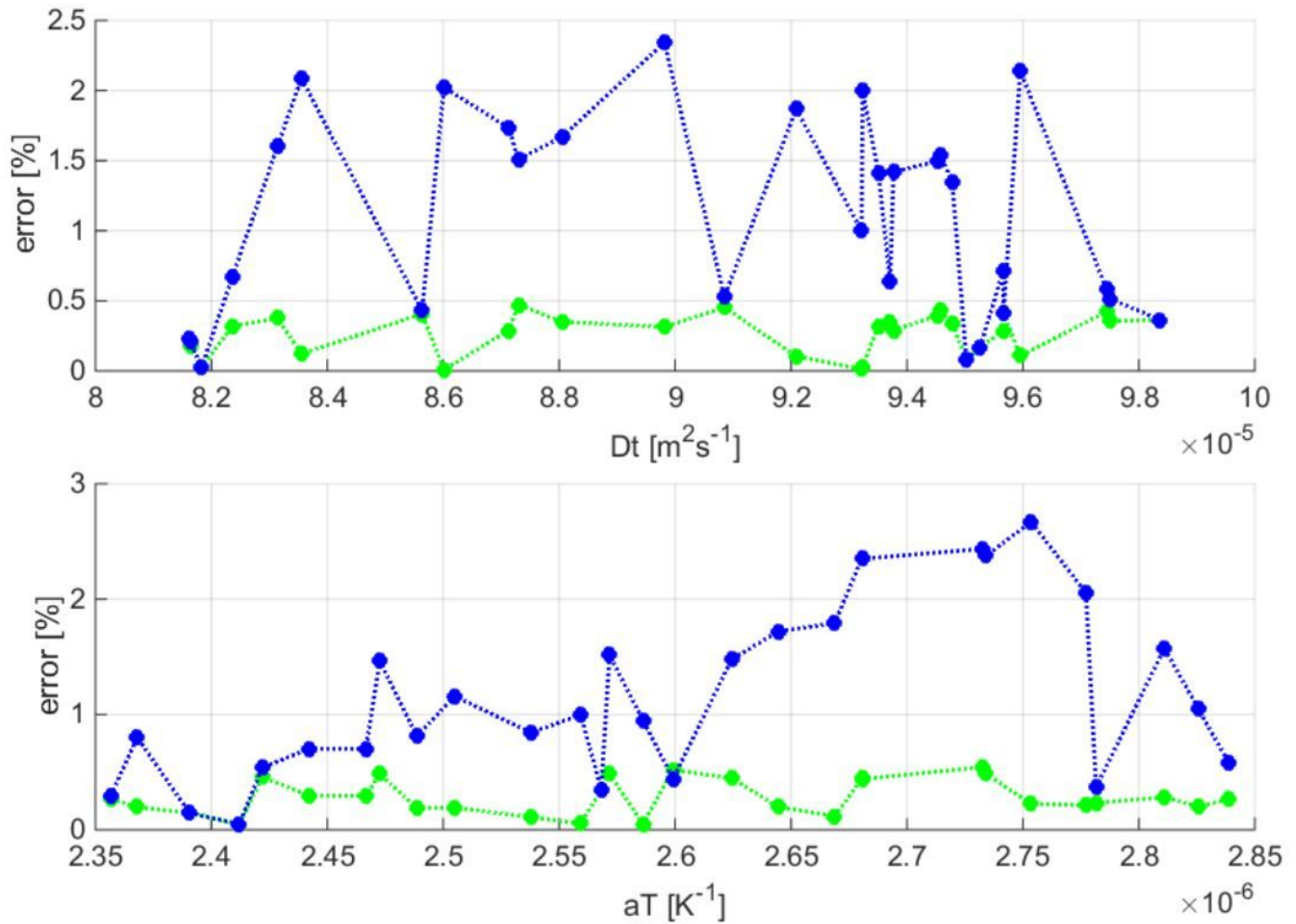


Figure 7

Relative errors of DT (up) and aT (down) obtained by the SCIP as the function of the corresponding parameter value preset by numerical experimental

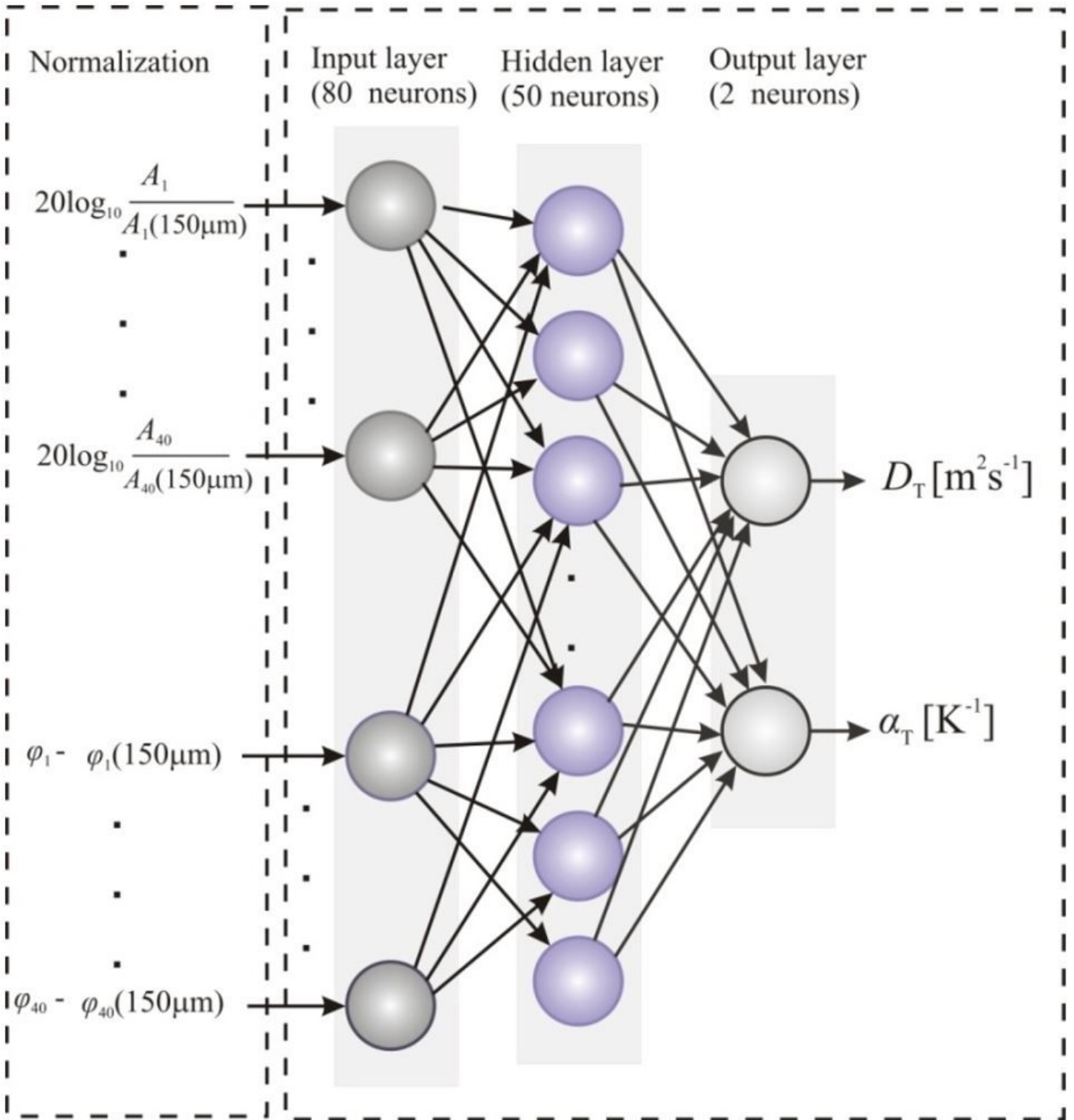


Figure 8

Neural network structure for inverse solution of photoacoustic problem for thermal diffusivity and expansion (2 output layer neurons) with normalized amplitude-phase signals (80 input layer neurons)

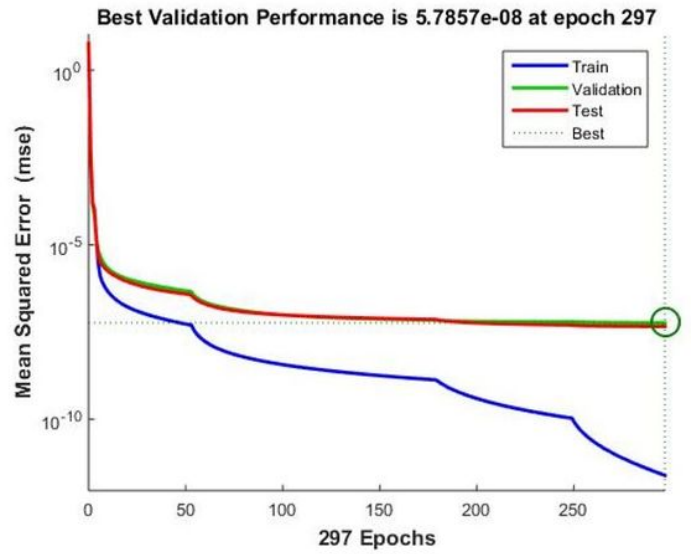
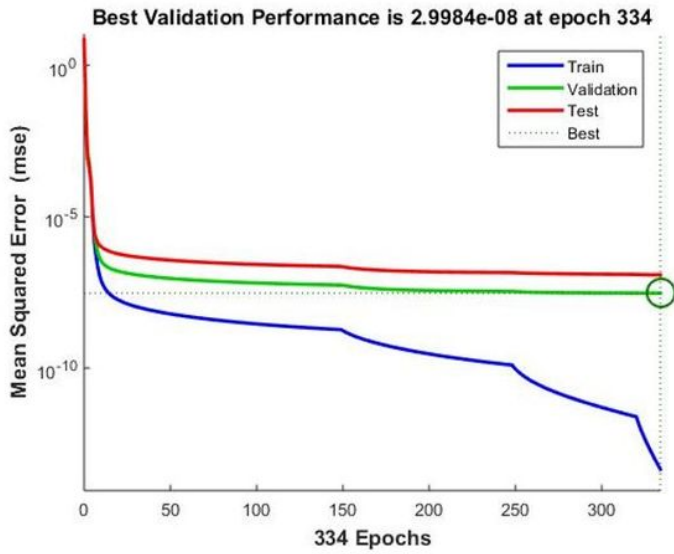


Figure 9

Training the neural network on two different bases with sample thickness of: a) 400µm and b) 900µm normalized with sample thickness of 150µm